

## *In Situ* Observation of Antisite Defect Formation during Crystal Growth

M. J. Kramer,<sup>1,2,\*</sup> M. I. Mendelev,<sup>1,†</sup> and R. E. Napolitano<sup>1,2,‡</sup><sup>1</sup>*Division of Materials Science and Engineering, Ames Laboratory, Ames, Iowa, 50011, USA*<sup>2</sup>*Department of Materials Science and Engineering, Iowa State University, Ames, Iowa 50011, USA*

(Received 30 June 2010; published 7 December 2010)

*In situ* x-ray diffraction (XRD) coupled with molecular dynamics (MD) simulations have been used to quantify antisite defect trapping during crystallization. Rietveld refinement of the XRD data revealed a marked lattice distortion which involves an *a* axis expansion and a *c* axis contraction of the stable *C11b* phase. The observed lattice response is proportional in magnitude to the growth rate, suggesting that the behavior is associated with the kinetic trapping of lattice defects. MD simulations demonstrate that this lattice response is due to incorporation of 1% to 2% antisite defects during growth.

DOI: 10.1103/PhysRevLett.105.245501

PACS numbers: 61.72.Bb, 61.72.Cc, 61.72.Dd, 61.72.jd

Crystallization of an undercooled liquid or glass is largely controlled by interfacial mechanisms between the growing crystals and the liquid that operate to accommodate the changes in both structure and composition across the boundary. To alleviate the kinetic burden of long-range transport, the pathways of highly driven (fast) crystallization processes may involve forming non-equilibrium structures [1] and compositions that arise from the trapping of defects such as excess solute atoms [2] or atomic-scale packing anomalies, such as vacancies, site-occupancy defects, stacking faults, etc. [3,4]. While the incorporation of these defects has been suggested by posttransformation analysis [5], they have not been well correlated with crystallization kinetics, and we are aware of no studies in which the formation of antisite defects during devitrification have been observed *in situ*.

Although direct observation of the formation of antisite defects is not possible at the present time, the investigation presented here demonstrates that indirect quantification of defect incorporation during crystallization can be achieved through *in situ* measurement of the lattice parameters through advanced x-ray methods [6,7]. The measurement of lattice parameter variation during devitrification has not yet been reported with accuracy sufficient to elucidate formation of site defects. This is primarily due to limitations in the accuracy and acquisition rate associated with *in situ* x-ray methods. In the present work, we use high energy x-ray diffraction and Rietveld analysis to overcome these experimental difficulties, and we employ molecular dynamics (MD) simulations for quantitative interpretation of the experimental data related to the concentration of antisite defect accumulated over the course of the devitrification. We choose as a test material the  $\text{Zr}_2\text{Cu}$  composition, a good glass-forming alloy [8] that crystallizes congruently to a *C11b* phase [9] from the liquid or from the glass [10] with no requirement for chemical partitioning or associated diffusion.

The  $\text{Zr}_2\text{Cu}$  alloy was prepared by arc melting pure Zr (99.95 mass %) and Cu (99.99 mass %) metals together

under ultrahigh-purity Ar. Amorphous ribbons ( $\sim 1 \times 0.040$  mm cross section) were obtained by melt-spinning on a copper wheel under ultrahigh purity He with a tangential speed of 25 m/s and  $1.6 \times 10^4$  Pa Ar overpressure. X-ray diffraction specimens were fabricated by placing  $\sim 10$  ribbon sections into a thin-walled silica tube ( $\sim 2$  mm diam) and sealing in Ar.

Time-resolved high energy x-ray diffraction experiments were performed at the 6-ID-D beam line (MUCAT) Advanced Photon Source (APS) at Argonne National Laboratory using monochromatic x rays with an energy of 99.55 keV, wavelength of 0.0124(6) nm. The distance from the sample to the detector was calibrated using NIST Si 640C standard providing a usable  $Q$  range of  $25 \text{ \AA}^{-1}$ . The forward scattered x rays were recorded at 0.5 Hz, using a GE CCD area detector with  $1024 \times 1024$  pixels per frame. Debye rings were integrated into 1D plots [11]. Samples were heated through crystallization at constant rates of 5 and 20 K/min. X-ray data were acquired in increments of 0.17 K from 570 to 670 K for the lower rate and 0.67 K from 300 to 870 K for the higher rate.

The fraction of the crystalline phase  $f$  was estimated in two ways: subtracting out the amorphous component of the data and fitting the amorphous phase concurrent with the crystalline phases using the GSAS Rietveld program [12]. Both methods resulted in identical crystalline phase fractions within statistical uncertainty. The whole pattern refinement difference (WRP) of less than 10% was achieved with  $f < 3\%$ , and WRP less than 5% was achieved with  $f > 10\%$  or more. The only other significant error was the placement of the sample relative to the detector which resulted in an absolute error of less than 1% for the lattice parameters between experiments.

The experimental data shown in Fig. 1 reveal six stages of devitrification. Stage I is characterized by the initial decrease in unit cell volume, reflecting the elastic response of the growing crystal, at low volume fraction, which forms under tension due to the higher atomic density compared to the parent glass. In stage II, both of the lattice parameters

increase as the normal thermal expansion of the crystalline phase becomes dominant. Stage III is characterized by very rapid crystallization with a concomitant increase in the unit cell volume associated with the fact that the growing crystal has higher atomic density compared to the parent glass. Stage IV begins at the completion of the crystallization transition, after which the material exhibits a rapid volume decrease, consistent with a viscous relaxation response of the residual glass to the rapid volume change associated with crystallization. In stage V, postcrystallization heating results in normal thermal expansion behavior until stage VI [insets of Figs. 1(b) and 1(c)], where continued heating is accompanied by both thermal expansion and a return to the equilibrium volume and  $c/a$  ratio for the C11b phase.

There are two main observations. First, we observe a significant change in both the unit cell volume and the individual lattice parameters for the C11b phase from the start of stage III to the completion of phase IV, indicating that the change in unit cell volume and the relative lattice response are more than transient elastic effects of the transition. Rapid crystal growth occurs after a substantial fraction of the original glass has crystallized [Fig. 2(a)], and is accompanied by a jump in the lattice parameters where the  $a$  axis lengthens and the  $c$  axis shortens [see  $\Delta a$  and  $\Delta c$  in Figs. 1(b) and 1(c); for the rest of the Letter, we will use the  $\Delta$  symbol only for the jump in the lattice parameters during rapid crystal growth]. Moreover, Fig. 2(b) shows that the magnitude of this lattice distortion increases with maximum in crystallization rate, as determined from the time dependence of the crystallized fraction [Fig. 1(a)]. A roughly constant crystallite number density observed through TEM analysis of quench-interrupted annealing specimens indicates that the rapid crystallization rate can primarily be attributed to growth, rather than nucleation. Second, while the unit cell volume exhibits nearly linear thermal expansion of  $2.80 \times 10^{-3} \text{ \AA}^3/\text{K}$  from  $\sim 675$  to  $775$  K, the individual axes have an unusual response, a decreasing  $a$  axis [inset of Fig. 1(b)] and accelerated increasing  $c$  axis with increasing temperature over the same temperature range [inset of Fig. 1(c)]. Below, we show that both of these observations can be explained by rate-dependent incorporation of antisite defects during fast crystal growth, followed by effective defect annealing at higher temperatures.

We now turn to MD simulation to examine the effect of point defects on lattice distortion. Our approach is to start with a perfect crystal model and to measure the change in lattice parameters resulting from random Cu-Zr site exchanges. For all MD simulations, we utilized a semi-empirical potential of the Finnis-Sinclair type [13], developed for the Cu-Zr system [14]. A constant volume and temperature ( $NVT$ ) scheme with periodic boundary conditions was used to model the B2 and C11b phases, with 24 334 and 17 424 atoms, respectively. In each case, the defects were introduced and the model was relaxed over a

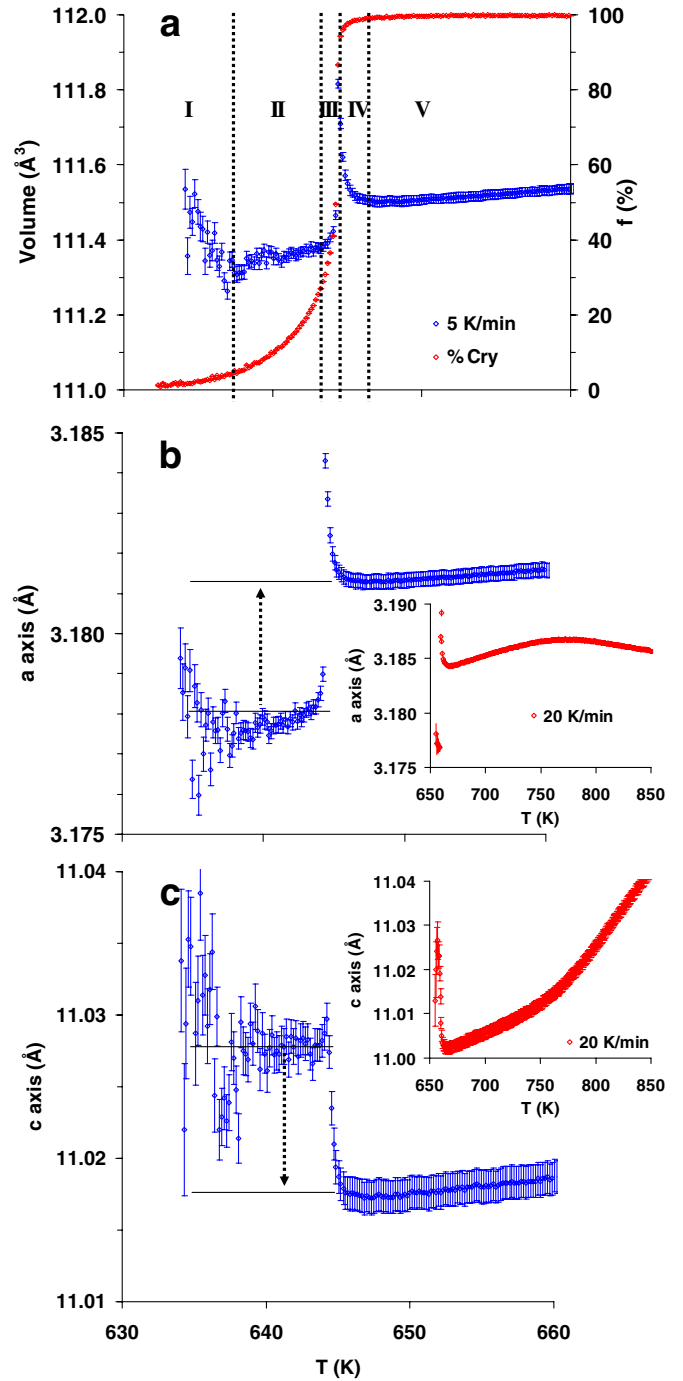


FIG. 1 (color online). Unit cell volume (a) and lattice parameters  $a$  axis (b) and  $c$  axis (c) as function of temperature for the heating rate of 5 K/min. The unit cell volume and the  $a$  axis both exhibit a jump in their thermal expansion during rapid growth while the  $c$  axis shows a decrease. The stages of crystallization for the heating rate 5 K/min are described in the text. The insets show the temperature dependences of the lattice parameters for the heating rate of 20 K/min. At 775 K the trends in lattice expansion for the  $a$  and  $c$  axes reverse.

periods of 20 000 MD steps (40 ps). Stresses were averaged over the next 20 000 MD steps, and the equilibrium lattice parameters were determined under the condition that all stresses are zero with uncertainties of  $<0.0001$   $\text{\AA}$ . Because

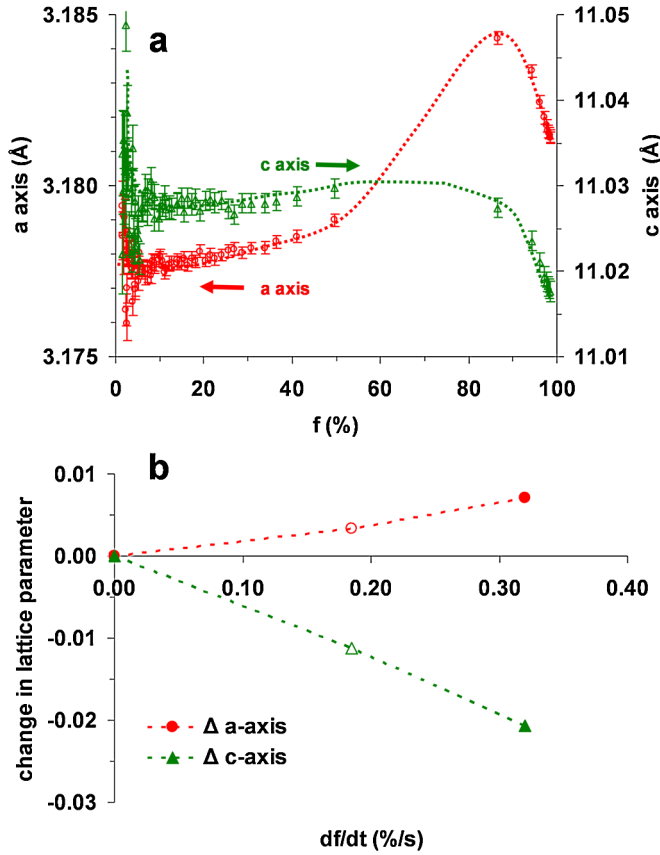


FIG. 2 (color online). The change in the *a* and *c* axes lattice parameters (a) as a function of the fraction crystallized (*f*) for the 5 K/min data set. The anisotropic changes in lattice as a function of the maximum in the growth rate (b) estimated for the 5 K/min (open symbols) and 20 K/min (closed symbols) data sets.

of the short duration of the simulations, chemical diffusion and defect annealing are not observed.

MD simulation results are summarized in Fig. 3. For the simpler *B2* case, the results show a modest increase in the lattice parameter with increasing number of antisite defects. This is not surprising since it is natural to assume that the most ordered system (perfect *B2*) will have the highest density. The more complicated *C11b* structure consists of *B2*-like units stacked in a staggered sequence along the *c* axis (Fig. 3, inset). As with the *B2* phase, increasing the antisite defects in the *C11b* phase should expand the basal-plane layers, increasing the *a* axis. Since the bonding between *B2*-like layers is of the Zr-Zr type, any replacement of Zr by the smaller Cu should lead to a decrease in the *c* axis. Both of these assertions are consistent with our MD results (Fig. 3).

Examining now the experimental findings in light of the MD simulation results, we make five specific points, as listed below.

(i) Experimental observation of the lattice distortion (*a* axis expansion and *c* axis contraction) during rapid growth [see Figs. 1(b) and 1(c)] are validated with MD simulation of the effect of antisite defects on the lattice parameters.

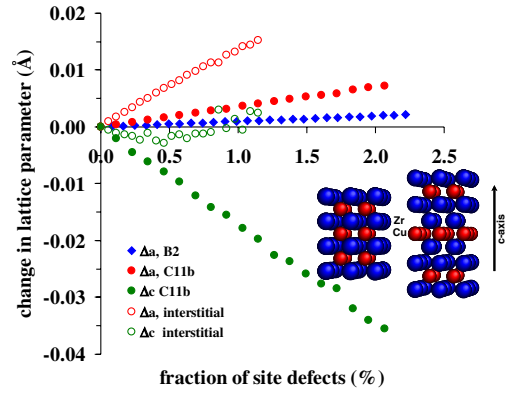


FIG. 3 (color online). Calculated changes in the lattice parameters as a function of site defects concentration using MD simulation. Open symbols are for interstitial and closed symbols for antisite defects. Diamonds are for the *B2* (cubic) phase and circles for *C11b*. Inset is an illustration of the *B2* and *C11b* structures showing the double Zr layer in between the Cu layers along the *c* axis. Swapping the smaller Cu for the larger Zr atoms is responsible for the contraction of the *c* axis and expansion of the *a* axis.

(ii) The relation between antisite defect concentration and lattice parameters, based on MD simulations, indicates that the increase in lattice distortion with increasing crystallization rate [Fig. 2(b)] can be attributed to increased incorporation of such defects in the growing crystal.

(iii) Experimentally measured changes in lattice parameter associated with rapid crystallization are  $\Delta a = 0.003(6)$  and  $\Delta c = -0.010(2)$  Å for heating at 5 K/min and  $\Delta a = 0.006(5)$  and  $\Delta c = -0.021(5)$  Å for heating at 20 K/min. Based on MD results (Fig. 3), these values correspond to defect concentrations of 0.6% to 0.9% and 1.2% to 1.8% for heating rates of 5 and 20 K/min, respectively. While this small defect density has an insignificant diffraction intensity, MD simulation demonstrates that the lattice response to this defect density is consistent with experiments.

(iv) The experimentally determined ratio of the tetragonal distortion,  $\Delta c/\Delta a$ , of  $-2.8$  and  $-3.5$  for heating rates of 5 and 20 K/min, respectively, are in line with MD simulation of  $\sim -4.8$ . It is significant that experiments and simulations both yield  $|\Delta c/\Delta a|$  ratio larger than unity and of the same order.

(v) The tetragonal distortion is relaxed when the sample is heated above 775 K. This further supports our assertion that the distortion is caused by the incorporation of antisite defects, which are annihilated by atomic transport at higher temperatures.

We now address the specific mechanisms by which the antisite defects may be formed. There are two possible scenarios. The antisite defects might be trapped because the glass-crystal interface moves so fast that the atoms do not have sufficient time to diffuse to an appropriate site. This is a purely kinetic effect. However, the antisite defects

might also appear because the glass density is smaller than the crystal density. Therefore, the crystal will grow under negative pressure  $p$ , serving to stabilize the lower-density, defect-rich structure. This is a thermodynamic effect which would increase the equilibrium antisite defect concentration by the factor of  $\exp(-pV_f/2kT)$ , where  $V_f$  is volume associate with the formation of 1 antisite defect pair and  $kT$  is the thermal factor. From the MD simulations, we find that  $V_f = 2.3 \text{ \AA}^3$ . Assuming that the difference between glass and crystal densities is  $\sim 4\%$  and the bulk modulus is  $\sim 100 \text{ GPa}$ , we estimate the pressure to be  $-4 \text{ GPa}$ , and the equilibrium antisite defect concentration should be increased by a factor of 1.7. The employed potential [14] predicts that the antisite defect formation energy is  $E_f = 1.74 \text{ eV/atom}$  at  $T = 650 \text{ K}$ , which results in the equilibrium antisite defect concentration of  $\sim 1.8 \times 10^{-7}$  (neglecting the formation entropy for the antisite defects). Therefore, the increase in the antisite defect concentration due to the thermodynamic effect can be  $1.8 \times 10^{-7} \times (1.7 - 1) = 1.2 \times 10^{-8}$ . As can be seen in Fig. 3, such a small change in the antisite concentration cannot explain the experimentally observed changes in lattice parameters. Therefore, the trapping of the antisite defects is a kinetic effect.

So far, we have considered only antisite defects, ignoring other point defects. MD simulations were used to estimate the effect of vacancies and interstitials. Two series of MD simulations were performed for the case of vacancies. In the first series, equal amounts of Cu and Zr atoms were removed from the simulation cell to create vacancies. In the second series only Zr atoms were removed to take into account that there can be some fraction of pure crystalline Zr in the sample. In these simulations, *both* the  $a$  and  $c$  axes decrease with addition of vacancies. Therefore, formation of vacancies cannot explain the experimental data, where  $\Delta c$  and  $\Delta a$  are of opposite sign. The effects of Cu interstitials were explored using 5 different types of “dumbbells” (oriented along [100], [001], [110], [101], and [111] directions). At  $T = 650 \text{ K}$  they all lead to qualitatively the same results shown in Fig. 3 for the [100] dumbbell: the  $a$  axis increases and the  $c$  axis decreases. While the trends are consistent, the details are not. First, in order to achieve the same magnitude of change in the experimental data ( $\sim 0.02 \text{ \AA}$ ), the interstitial concentration exceeds 1%, which is unrealistic. Second, the change in the  $a$  axis is much larger than the  $c$  axis while experimentally the change in the  $c$  axis is  $\sim 3$  times larger than the  $a$  axis. Third, the dependence of the  $c$  axis on concentration has a minimum at  $\sim 0.003 \text{ \AA}$ , while the experimentally observed change in the  $c$  axis is 6 times larger.

In conclusion, we show that in an ideal system where the phase selection is the thermodynamically stable phase and long-range diffusion is not required, the lattice response to crystal growth can be complex. In the  $\text{Zr}_2\text{Cu}$  alloy studied, the  $a$  axis expands while the  $c$  axis contracts during rapid growth. Transient response in lattice parameters is consistent with  $\sim 1\%$  antisite defects. In fact, in addition to novel response of the lattice, we report a new approach for quantifying antisite defect formation during fast crystal growth, where *in situ* time resolved x-ray diffraction can provide high quality data on the change in lattice parameter during the crystal growth, while MD simulation provides an accurate means to quantify the antisite defect concentration.

The authors gratefully acknowledge useful discussions with Professor P. A. Thiel and the assistance of M. Xu on sample preparation, I. Kalay on DSC, and E. Kalay on TEM. This work was supported by the U.S. Department of Energy, Office of Basic Energy Science, Division of Materials Sciences and Engineering. Ames Laboratory is operated for the U.S. DOE by Iowa State University under Contract No. DE-AC02-07CH11358. Use of the Advanced Photon Source was supported under Contract No. DE-AC02-06CH11357.

---

\*mjkramer@ameslab.gov

†mendelev@ameslab.gov

‡ralphn@iastate.edu

- [1] H. Reichert *et al.*, *Nature (London)* **408**, 839 (2000).
- [2] W.J. Boettinger and M.J. Aziz, *Acta Metall.* **37**, 3379 (1989).
- [3] J. Fan *et al.*, *Phys. Rev. E* **74**, 031602 (2006).
- [4] J.C. Ramirez and C. Beckermann, *Acta Mater.* **53**, 1721 (2005).
- [5] W. Kurz, *Adv. Eng. Mater.* **3**, 443 (2001).
- [6] G. Sankar, J. M. Thomas, and C. R. A. Catlow, *Top. Catal.* **10**, 255 (2000).
- [7] J.F. Loffler and W.L. Johnson, *Mater. Sci. Eng. A* **304**, 670 (2001).
- [8] Z. Altounian, G.H. Tu, and J.O. Stromolsen, *J. Appl. Phys.* **53**, 4755 (1982).
- [9] D. Arias and J. P. Abriata, *Bull. Alloy Phase Diagrams* **11**, 452 (1990).
- [10] M.J. Kramer *et al.*, *Metall. Mater. Trans. A* **39**, 1847 (2008).
- [11] A. P. Hammersley *et al.*, *High Press. Res.* **14**, 235 (1996).
- [12] A. C. Larson and R. B. V. Dreele, Los Alamos National Laboratory Report No. LAUR 86-748, 2004, p. 231.
- [13] M.W. Finnis and J.E. Sinclair, *Philos. Mag. A* **50**, 45 (1984).
- [14] M.I. Mendelev *et al.*, *Philos. Mag.* **89**, 967 (2009).